JTTEE5 4:235-244

Effect of Starting Powders on the Control of Microstructural Development of Al-Cu-Fe Quasi-Crystalline Plasma-Sprayed Coatings

D.J. Sordelet, M.J. Kramer, and O. Unal

Powders and plasma-sprayed coatings of an $Al_{63}Cu_{25}Fe_{12}$ alloy containing a quasi-crystalline phase were characterized by X-ray diffraction, electron microscopy, and differential thermal analysis. The relationships between powder and coating microstructures were examined. Powders were produced by casting and crushing and by gas atomization. Both techniques produced powders with multiple phases; cubic and monoclinic ternary structures were formed along with the face-centered icosahedral quasi-crystalline phase. These phases were also produced in the plasma-arc-sprayed coatings formed using different starting powders. Cooling rates during powder processing greatly affected the phase equilibria and scale of segregation of this alloy. Finer grain sizes in the plasma-sprayed coatings were obtained from the more chemically homogeneous gas-atomized powders.

1. Introduction

QUASI-CRYSTALS have fivefold rotational symmetries (previously forbidden by classical laws of crystallography), but do not exhibit long-range translational symmetry. More than 100 alloy systems have been identified to contain a quasi-crystalline phase. This new class of materials, fitting somewhere between amorphous and crystalline materials, has many fascinating properties. Quasi-crystals formed in the Al-Cu-Fe system are among the few alloys to have been studied in terms of several of their physical properties, such as hardness, thermal expansion, and thermal conductivity. Al-Cu-Fe quasi-crystals have low density (4 to 5 g/cm^3), high hardness (600 to 1000 kg/mm^2), and a high elastic modulus (70 to 100 GPa) (Ref 1). The high hardness combined with a high elastic modulus indicates a good ability for elastic recovery as well as the capacity to absorb impact energy under contact deformation (Ref 1).

Previous studies have also shown that Al-Cu-Fe quasi-crystalline alloys have favorable wear resistance and low friction properties, but the performance of these coatings is compromised by a coarse, heterogeneous microstructure (Ref 2, 3). The objective of the current study is to compare the chemical uniformity and the microstructure of starting powders produced by different techniques with characteristics of the resulting plasma-sprayed coatings in an attempt to produce a finer, more homogeneous microstructure.

The microstructures and properties of thermal spray coatings can be altered by varying the preparation techniques used to produce the feedstock powders. The chemical uniformity and morphology of powders strongly influence the physical and chemical properties of thermal spray coatings. Kubel (Ref 4) reviewed a variety of powder manufacturing methods and focused on the impact of chemical uniformity and particulate morphology on nickel-aluminum coating characteristics. Other studies have consistently demonstrated that very fine-scale chemical uniformity and spherical powder morphology produce improved coating properties (Ref 5-7). For example, oxidation or corrosion rates may be accelerated due to phase segregation in the alloy coating, especially if chemical inhomogeneities produce localized anodic and cathodic sites (Ref 8). Mechanical properties, such as wear resistance or thermal cycling fatigue resistance, may be compromised by lower coating densities induced by poor powder morphologies.

Processing of feedstock powder may involve solidification (e.g., atomization or ingot casting followed by crushing) or solid-state reactions (e.g., spray drying followed by sintering). In the atomization processes, a superheated melt stream is disintegrated and rapidly solidified using water or gas jets, resulting in an Gaussian distribution of powder sizes. Morphologies of atomized powders range from primarily spherical for gas atomized to irregular for water atomized. The very high cooling rates of atomization processes tend to produce high chemical uniformity for alloyed systems. Casting of materials followed by crushing into powder is frequently used to produce powders of ceramics and brittle metal alloys, which are not readily produced by atomization processes. Casting and crushing of alloys suffers from large-scale chemical segregation due to low cooling rates; furthermore, powder morphologies developed through crushing are typically angular and very irregular.

Keywords: Al-Cu-Fe alloys, plasma spraying, quasi-crystals

D.J. Sordelet, M.J. Kramer, and **O. Unal,** Ames Laboratory, U.S. Department of Energy, Iowa State University, Ames, IA 50011, USA

2. Experimental Procedures

2.1 *Starting Powders*

A starting composition of $Al_{63}Cu_{25}Fe_{12}$ was used throughout this study. This composition falls within the quasi-crystalline (ψ) single-phase region of the phase diagrams determined by Gayle et al. (Ref 9) and Gratias et al. (Ref 10). For the casting and crushing method, a 5 kg ingot was prepared by induction melting a mixture of aluminum (99.999), copper (99.99), and iron (99.99) in an alumina crucible under an argon atmosphere. The melt was heated to 1100 °C and held for 15 min before being

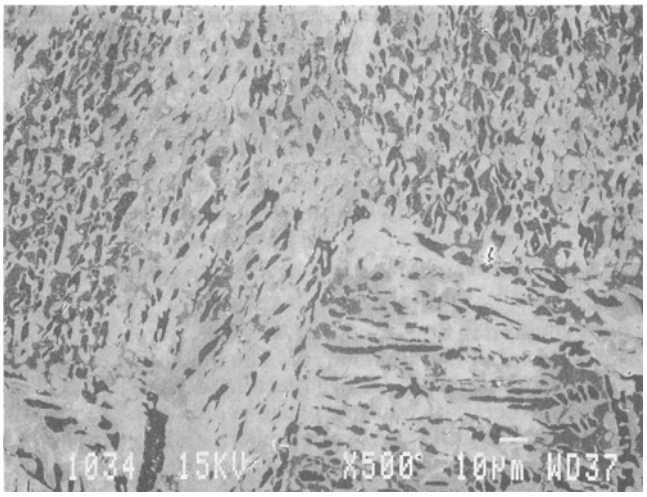

(a)

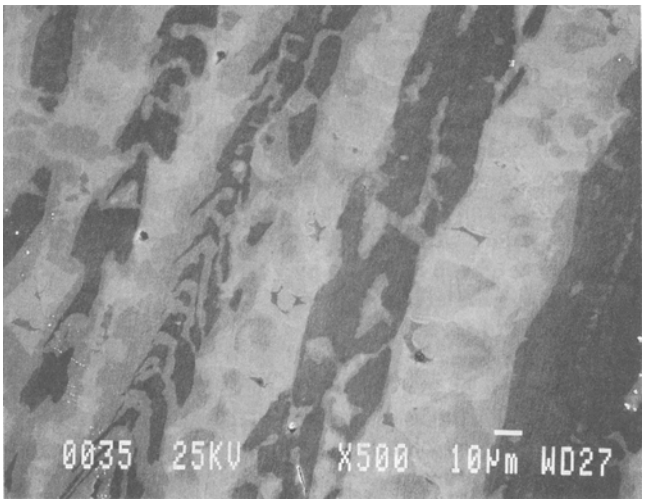

(b)

Fig. 1 SEM micrographs (secondary electrons) of polished cross sections of $Al_{63}Cu_{25}Fe_{12}$ cast ingot. (a) From outer rim region of ingot. (b) From center region of ingot

Table 1 Plasma spraying parameters used for CC and GA $Al_{63}Cu_{25}Fe_{12}$ powders

Gun	Miller Thermal SG-100 (Miller Thermal Inc., Appleton, WI)
Anode	2083-358 (mach I mode)
Cathode	112
Gas injection	113
Current, A	800
Voltage, V (at gun)	43.6
Arc gas (Ar) flow rate, SLPM	37.8
Auxiliary gas (He) flow rate, SLPM	20.0
Powder carrier gas (Ar) flow rate, SLPM	5.6
Powder feed rate, g/min	20.0
Spray distance, cm	7.5
Powder size, µm	+5,–45

bottom-poured into a water-chilled 5 cm diam by 50 cm long copper mold. The cast ingot was subsequently fractured into smaller pieces and then ground in a motorized agate mortar and pestle. The ground powder was air classified into a distribution between 5 and 45 µm for plasma spraying. Prior to fracturing the cast ingot, a 1 mm thick wafer was cut from the midsection of the ingot for characterization of the as-cast microstructure.

The second powder was prepared by a gas atomization technique. Similar starting material purities were employed. Following powder synthesis, the powder was air classified to yield a +5, –45 µm size distribution. The two powder-processing techniques used in this study allowed examination of two extremes in solidification rates. Throughout this paper, the terms CC and GA will refer to the cast and crushed powder and the rapidly solidified gas-atomized powder, respectively.

2.2 *Plasma Spraying Process*

Air plasma spraying was performed using a Miller thermal SG-100 gun (Miller Thermal, Inc., Appleton, WI). Mild steel substrates were degreased and grit blasted with 24-grit Al_2O_3. Two coating thicknesses of each powder were prepared, ~200 and ~800 µm, to assess coating microstructure effects related to differences in cooling rates of the coatings. Plasma spraying parameters were briefly evaluated to achieve reasonably dense microstructures (Table 1). These conditions were used with both the CC and GA powders.

Metallographic samples of the plasma-sprayed coatings were prepared by mounting a cut section of the coated steel substrate in epoxy and sectioning with a low-speed diamond saw. The blade entered the coating and exited through the back of the substrate to help prevent spallation. Grinding and polishing were performed on an automatic system using an initial 180-grit SiC paper followed by 9 and 3 µm diamond lapping. A final polish with 0.05 µm Al_2O_3 was employed to remove scratches, particularly in the substrate.

2.3 *Characterization Techniques*

The compositions of the starting powders and plasma-sprayed coatings, after removal from the substrates, were measured by the inductively coupled plasma/atomic emission spectroscopy (ICP/AES) technique. Oxygen contents of the same materials were determined by inert gas fusion.

The compositions of the phases formed in the cast ingot were determined using an ARL SEMQ (Applied Research Laboratories, Sunland, CA) electron microprobe. Standard samples of high-purity aluminum, copper, and iron were prepared by the Materials Preparation Center of the Ames Laboratory for standardization of background spectra used in the electron microprobe (EMP) analysis. At least 20 measurements were taken of each phase in the bulk sample cut from the ingot midsection.

X-ray diffraction (XRD) was performed with a Philips 1810 diffractometer (Philips Electron Instruments, Inc., Mahwah, NJ) using CuK_α radiation to qualitatively characterize the phases in the cast ingot, starting powders, and plasma-sprayed coatings. The cast ingot section and starting powders were X-rayed in their existing form, whereas plasma-sprayed coatings were ground to eliminate any texturing effects.

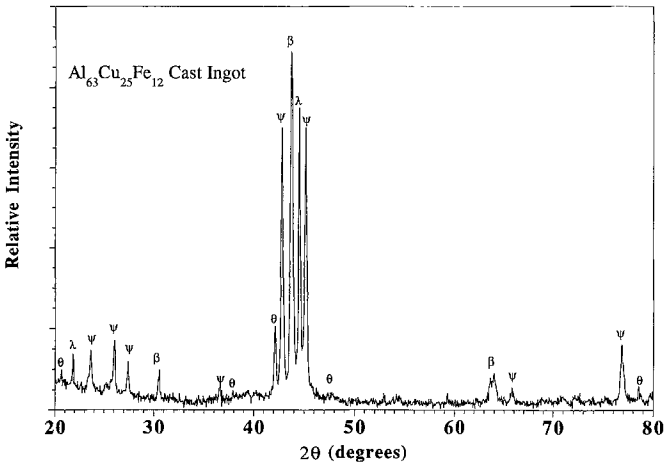

Fig. 2 XRD pattern of bulk specimen cut from $Al_{63}Cu_{25}Fe_{12}$ cast ingot

The as-solidified microstructures of the cast ingot, GA powder, and plasma-sprayed coatings were observed with a JEOL 6100 scanning electron microscope (SEM) (JEOL Ltd., Medford, MA) and a Philips CM30 transmission electron microscope (TEM).

For planar sections of the plasma-sprayed coatings, 3 mm disks were electrospark-cut from the coated substrates and mechanically ground and polished from the substrate side to approximately 50 μm thick, with the result that only the near top surface of the coating was investigated. For cross sections, two small pieces of coating were epoxied face-to-face and mechanically thinned to 50 μm. Ion milling to perforation was performed at 3 kV using a liquid-nitrogen-cooled stage to minimize milling damage.

Differential thermal analysis (DTA) was performed to compare the thermal events on heating of the CC and GA powders as well as the plasma-sprayed coatings prepared from the two powders. The DTA results were obtained with a Perkin-Elmer System 7 unit (Perkin-Elmer Corp., Norwalk, CT). Scans were performed in flowing argon using a heating rate of 10 °C/min and samples of ground powder weighing approximately 50 mg.

3. Results

3.1 *Cast Ingot*

The solidification microstructure of the $Al_{63}Cu_{25}Fe_{12}$ ingot is shown in Fig. 1. Three phases are clearly visible. The dark phase exhibiting a dendritic morphology appears to have solidified first, followed by the medium gray phases surrounding the dendrites. Finally, the light gray phase appears to have formed from the final interdendritic liquid. The contrasting cooling rates between the inner and outer regions of the cast ingot are manifested in the resulting scale of segregation. The microstructure of the inner ingot region (Fig. 1b) is characterized by larger grains than the outer region (Fig. 1a), which cooled more rapidly due to the chilling of the water-cooled copper mold wall. The two regions appear to differ only in grain size, not in the number

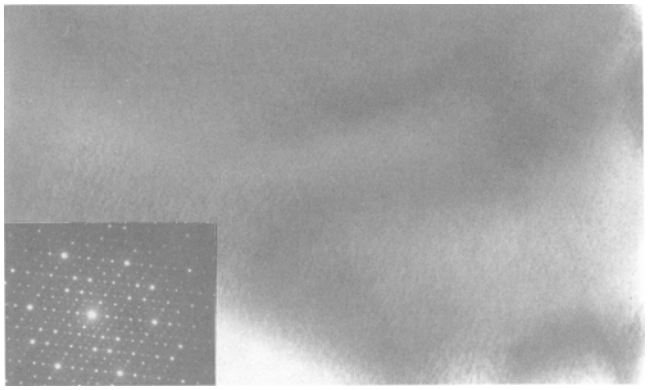

(a)

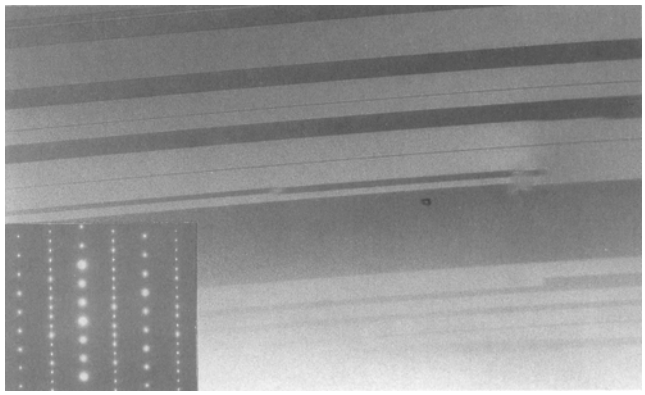

(b)

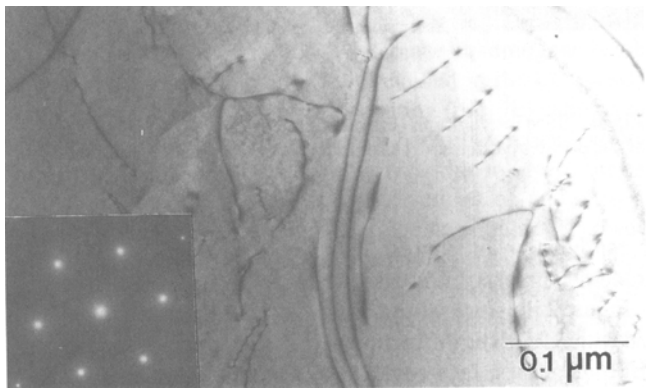

(c)

Fig. 3 Bright-field TEM micrographs of selected grains in bulk specimen cut from $Al_{63}Cu_{25}Fe_{12}$ cast ingot. (a) Corresponds to the medium gray phase in Fig. 1. This is the ψ phase, showing few defects. The selected-area diffraction pattern (SADP) inset is for a twofold zone axis showing rotational but lacking translational symmetry. (b) Corresponds to the medium dark gray phase in Fig. 1. This is the λ phase, which is characterized by numerous twin lamellae. The SADP inset is for a [110] zone axis projection. (c) Corresponds to the light gray phase in Fig. 1. This is the β phase, showing numerous defects. The SADP inset is for a [111] zone axis projection

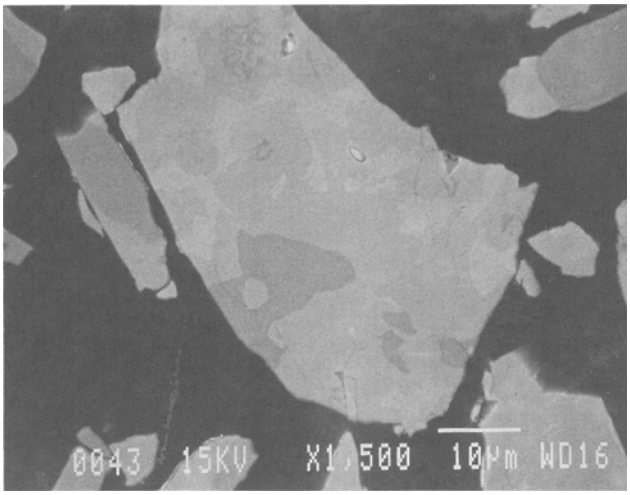

(a)

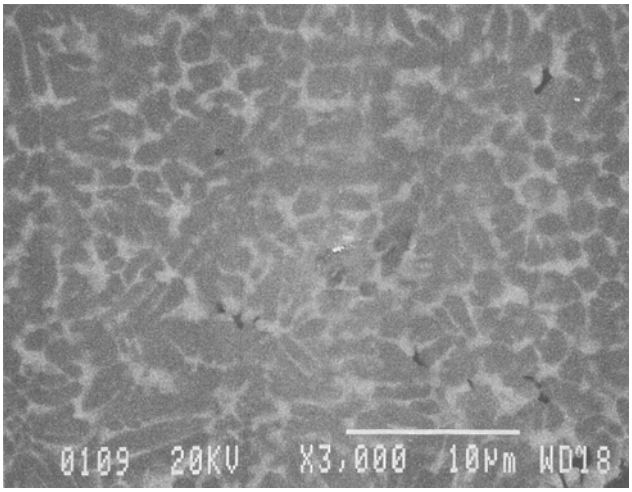

(b)

Fig. 4 SEM micrographs (backscattered electrons). (a) Cross section of CC powder particles. (b) Cross section of GA powder particles

or composition of phases. This was confirmed by EMP and structural analysis, as discussed later.

Figure 2 illustrates the phases in the cast ingot section identified with XRD. The diffraction patterns were determined to contain four phases: face-centered icosahedral $Al_{63}Cu_{25}Fe_{12}$ (ψ), monoclinic $Al_{13}Fe_4$ (λ), cubic AlFe (β), and tetragonal Al_2Cu (θ); the latter three phases are isostructural with these stoichiometric compounds. However, as discussed later, these phases were found to be ternary compounds. The monoclinic, cubic, and tetragonal phases have the *C2/m*, *Pm*$\bar{3}$*m*, and *I4/mcm* space groups, respectively. The peaks originating from the quasi-crystalline phase (ψ) are associated with the face-centered icosahedral structure. These results are in agreement with the work of Gayle et al. (Ref 9). According to the isothermal sections of the Al-Cu-Fe phase diagram proposed by Gayle et al., the $Al_{63}Cu_{25}Fe_{12}$ composition does not melt congruently and should reside in a single-phase face-centered icosahedral region. Clearly, equilibrium was not achieved in the cast ingot, nor would one expect it to under these conditions. The presence of the θ phase was not observed in the SEM micrographs or detected with EMP. This phase is the lowest-melting phase present. Therefore, it is likely to be uniformly distributed throughout the very fine interdendritic regions. In addition, the θ phase is chemically similar to β, making detection more difficult, particularly in a secondary electron image.

Table 2 Characterization of $Al_{63}Cu_{25}Fe_{12}$ cast ignot

Phase region	Symbol designation	Composition	Crystal structure
Medium gray	ψ	$Al_{64}Cu_{24}Fe_{12}$	Face-centered icosahedral
Dark gray	λ	$Al_{72}Cu_5Fe_{23}$	Monoclinic
Light gray	β	$Al_{55}Cu_{40}Fe_5$	Cubic

The approximate compositions of the phases shown in Fig. 1 were determined by EMP analysis. The results are displayed in Table 2, along with the corresponding crystal structures of the phases. The description of phases based on gray scales refers to the SEM micrographs in Fig. 1. Grains from the inner and outer ingot sections were analyzed, but no significant compositional differences were observed as long as sufficiently large grains were selected.

A sample from the cast ingot section was observed in TEM. Figures 3(a), (b), and (c) show TEM micrographs corresponding to the ψ, λ, and β phases, respectively. A twofold diffraction pattern for the ψ phase, a [110] pattern for the λ phase, and a [111] pattern for the β phase are included as insets to the micrographs. It is clear from Fig. 3 that the three phases have distinctive morphological features. Quasi-crystal grains generally have no defects or bend contours, indicating that they are brittle and that dislocation activity is not favored. On the other hand, intermetallic phases of λ, which twins on the (001) planes, and β contain distinct planar defects and dislocations, respectively. Identification of phases was made by a systematic study of electron diffraction patterns. Energy-dispersive spectroscopic (EDS) studies were also made, but although the findings were generally in agreement with the EMP findings presented earlier, EDS was inconclusive for identification purposes due to the large solubility of copper in AlFe. Unequivocal identification of the crystal structure and chemistry of specific grains seen in Fig. 1 was thus made by comparing the results of electron diffraction, XRD, and EMP studies. The composition of the ψ phase is very close to the starting composition, $Al_{63}Cu_{25}Fe_{12}$. The λ phase has an approximate stoichiometry of $Al_{13}Fe_4$. On the other hand, the β phase is far from the AlFe composition. Gayle et al. (Ref 9) reported that this structure has a large solubility for copper. Their results with varying compositions confirmed that up to 45% Cu can be accommodated by the β structure, along with iron and aluminum. The copper substitution observed in β results in an increase in the lattice parameter by approximately 1.1%.

3.2 *Starting Powder*

The microstructure of the CC powder is very similar to the microstructure of the starting ingot (Fig. 1). Figure 4(a) shows the distribution of phases shown throughout the crushed parti-

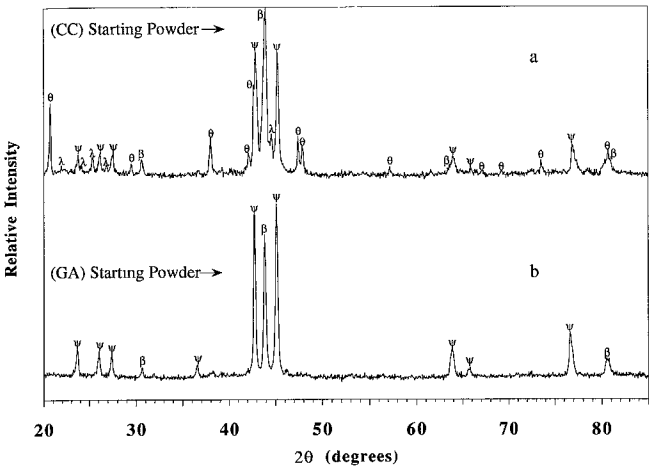

Fig. 5 XRD patterns of CC powders (a) and GA powders (b)

cles. The cross-sectional microstructure of the GA powder is shown in Fig. 4(b). The effects of the high cooling rates operative in preparing the GA powder are clearly visible. There is still some segregation present in the GA powder, but the scale is much less than the CC powder and precluded chemical analysis by traditional EMP.

The phases detected in the CC and GA powders by XRD are shown in Fig. 5. Comparing the trace from the CC powder in Fig. 5(a) to the trace obtained from the cast ingot bulk section (Fig. 2) reveals two interesting differences. First, the powder sample shows more of the θ phase. Second, the relative intensities of the θ and λ phases are quite different. The first difference is likely due to sampling differences. The cast ingot bulk section, which was cut prior to crushing and grinding, represents a very small percentage (<1%) of the entire ingot. Conversely, the powder sample is much more likely to represent all the phases present in the ingot. With the large-scale segregation exhibited by the peritectic-forming phases, it is likely that the small cast ingot bulk section had an uncharacteristically small fraction of the θ phase. The discrepancies between the relative intensities of the θ and λ phases are most likely the result of texturing in the cast ingot bulk specimen. The low symmetries of the tetragonal θ and monoclinic λ typically produce preferred orientation in solidification methods with slower cooling rates.

The GA powders show two primary phases: β and ψ. Also, the GA powders qualitatively appear to have a higher ψ phase content with the CC powder. However, this judgment by comparing peak heights is very suspect, particularly considering the complex atomic structure and scattering phenomena associated with the quasi-crystalline ψ phase.

3.3 *Plasma-Sprayed Coatings*

Plasma spraying parameters were adjusted to produce coatings that were relatively dense in appearance. Individual splats were analyzed to observe the melting and projection behavior of the CC and GA powders. Figure 6(a) shows a typical splat morphology produced with the CC powder using the parameters described in Table 1. The extremely fine grain structure of the CC splat after removal from the substrate is seen in the TEM micrograph in Fig. 6(b). Coating micrographs in subsequent figures will demonstrate the substantial grain coarsening that occurs during plasma spray deposition.

Table 3 Chemical analysis of CC and GA powders and plasma-sprayed coatings

Sample	Al, at.%	Cu, at.%	Fe, at.%	O, ppm by weight
CC starting powder	63.5	24.8	11.7	591
Ga starting powder	64.3	25.0	10.7	438
Thin coating, CC powder	61.7	26.1	12.1	7844
Thick coating, CC powder	60.6	27.1	12.3	...
Thin coating, GA powder	62.3	26.0	11.8	9544
Thick coating, GA powder	60.9	26.6	12.5	...

Chemical analyses of the CC and GA powders and plasma-sprayed coatings are presented in Table 3. The nominal composition of $Al_{63}Cu_{25}Fe_{12}$ is retained by the powders, but the coatings have shifted away from the initial composition. The splats in Fig. 6(a) and (b) are indicative of a very well-melted particle; selective vaporization of aluminum may have caused the deviation in the composition of the coating. Oxygen levels for the CC and GA powders are comparable. During plasma spraying, some oxidation occurs, with roughly one order of magnitude increase in oxygen. These levels are far too low to detect by XRD. Distinct oxide particles were not detected in TEM; however, the oxygen is probably present as a metallic oxide surface film on prior splat boundaries rather than as an interstitial solution or a precipitated oxide phase.

Polished cross sections of coatings formed with CC and GA powders are shown in Fig. 7. The coarse inhomogeneity observed in the cast ingot (Fig. 1) is retained in the CC powder coating (Fig. 7a). The GA powder coating (Fig. 7b) exhibits far less chemical segregation. While the benefits to chemical uniformity of the GA powders are clearly visible in Fig. 7, the expected differences in porosity and fractions of unmelted or partially melted particles using the irregular, angular CC powder and the more desirable spherical morphology of the GA powder were not observed. Additional work is needed to tailor the plasma spraying parameters for this composition and particle size to produce denser coatings.

X-ray diffraction patterns obtained from plasma-sprayed coatings prepared with the two different powders are shown in Fig. 8. The patterns were obtained from the thick coatings; however, the patterns from thin CC and GA powder coatings were nearly identical. The quasi-crystalline ψ and crystalline β phases are clearly visible in both coatings. The CC powder coating shows no reflections from the θ phase present in the starting powder (Fig. 5). The λ phase is not easily identified in Fig. 8. As discussed earlier, this latter observation may be due to the similar *d*-spacings of the highest intensity peaks corresponding to the ψ, β, and λ phases.

Bright-field imaging and electron diffraction of the plasma-sprayed coatings provided an interesting complement to the

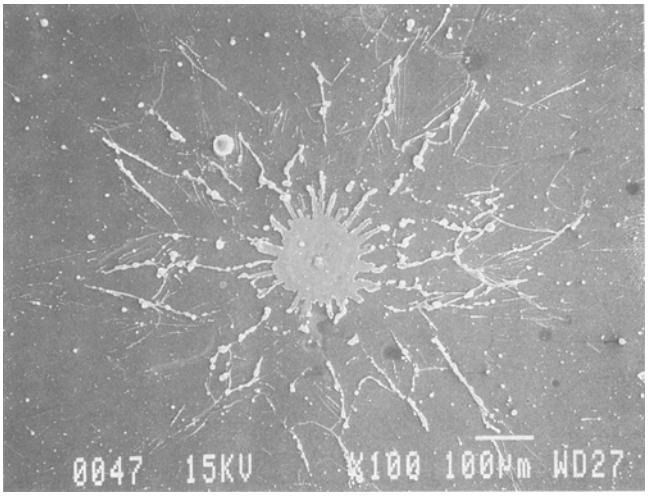

(a)

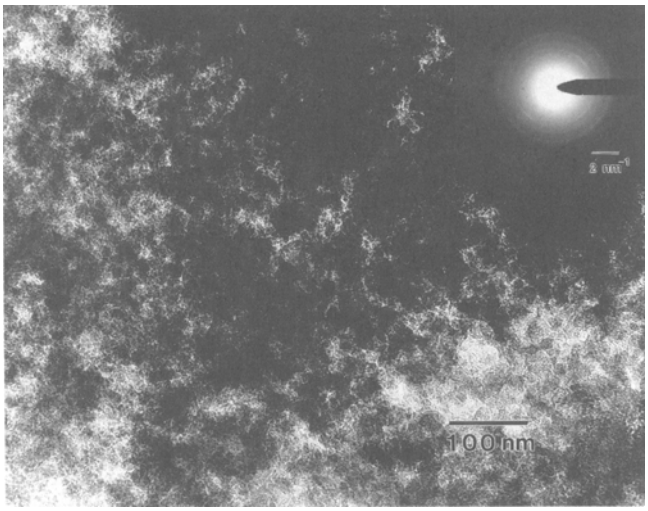

(b)

Fig. 6 (a) SEM micrograph (secondary electrons) of individual splat of CC powder particle. (b) Bright-field TEM image from center area of splat shown in (a). The inset is a SADP of this area that indexes to a simple cubic structure, with $a_0 = 0.41$ nm

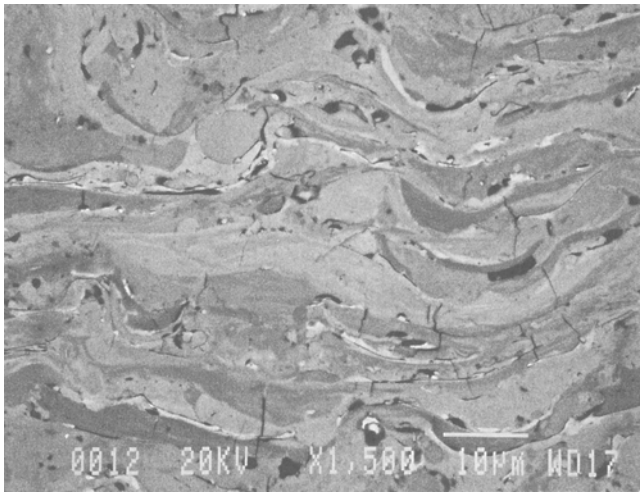

(a)

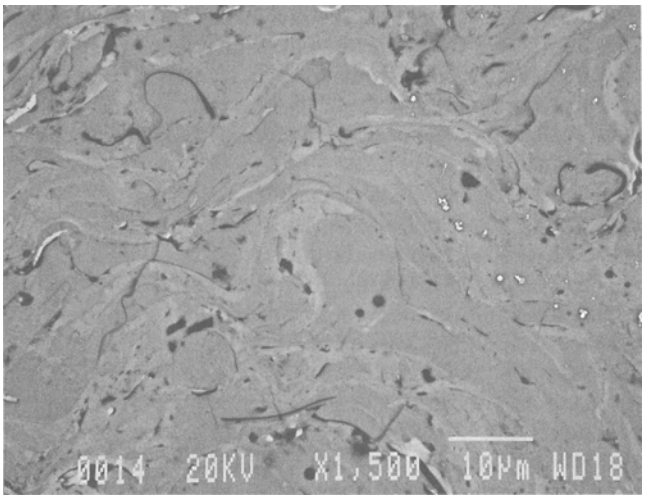

(b)

Fig. 7 SEM micrographs (backscattered electrons) of polished cross sections of plasma-sprayed coatings formed with CC powders (a) and GA powders (b)

bulk XRD information. Figure 9 shows several representative TEM micrographs obtained from CC and GA powder coatings. Note that images from the GA coating are shown in both a planar section (i.e., parallel to spray direction) and a cross-sectional view (i.e., normal to spray direction). Figure 9(a) shows that in the CC coating the crystalline phases, particularly λ, have a grain size larger than 1 µm. The ψ phase grain size generally tends to be smaller than 1 µm. This is clearly visible in the SADP in Fig. 9(a) (inset), in which a continuous ring pattern is observed for the ψ phase whereas only a single off-zone axis pattern that indexes to the λ phase is observed when using a 10 µm aperture. The λ phase in Fig. 9(a) has a structure identical to that shown in Fig. 3(b). For the GA coatings, all grains tend to be submicron (Fig. 9b). Analysis by TEM/EDS reveals that the λ and ψ grains have nearly the same compositions as those determined by EMP for the as-cast ingot. The compositions determined by EDS from the TEM specimens are given in Table 4. The β phase was not observed in EDS in this region, but diffraction spots were identified (Fig. 9b, inset). Careful analysis of an electron diffraction pattern obtained from broad areas (i.e., 50 to 100 µm) demonstrated that the β phase does indeed occur in the plasma-sprayed coatings, as also seen in XRD (Fig. 8b).

Figure 9(c) shows a typical cross section of the GA coating. The only obvious difference in the cross sections compared to the planar views are the narrow aluminum-rich regions (~10 nm wide) between polyphased sections up to 2 µm across. Although these regions were amorphous, it is not known whether they represent elemental aluminum or an oxide phase because the EDS detector used has a thick beryllium window and cannot detect oxygen. The size and approximate cross-sectional area of these regions are consistent with the expected size of a single splat, and thus the aluminum-rich regions may be the boundary area between the individual splats. Although not specifically ana-

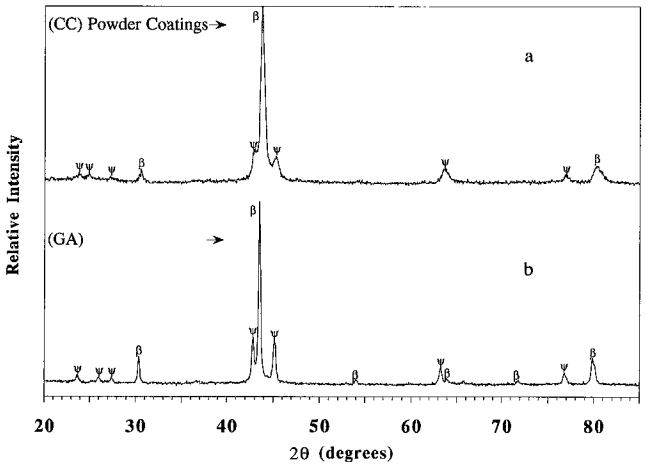

Fig. 8 XRD patterns of plasma-sprayed coatings formed with CC powders (a) and GA powders (b)

lyzed in this study, the aluminum-rich areas may be splat surface oxides formed during spraying. Estimation of the oxygen contribution of a 10 nm thick Al_2O_3 skin that forms on a splat produced from a 25 μm diam sphere is within one order of magnitude of the oxygen levels measured from the plasma-sprayed coatings.

Due to the numerous overlapping peaks and different X-ray scattering factors for the various phases seen in the XRD and SADP data, DTA was used in an attempt to provide a more sensitive indication of the presence of minor phases and their relative properties. Figure 10 illustrates the DTA traces for the CC and GA powders. It is readily seen that the CC powder has more exothermic transitions with stronger signatures than the GA powder. The first strong exothermic reaction near 600 °C appears to be the peritectic decomposition of the θ phase to liquid and a tetragonal Al_7Cu_2Fe (ω) phase (Ref 11). The ω phase decomposes at around 710 °C and is followed by melting of the ψ phase near 840 °C. Since the ω phase is transient, it did not appear in the XRD patterns of the CC powder. Curve (b) in Fig. 10 shows only a slight indication of the above reactions for the GA powders, confirming the increased homogeneity of these powders. After plasma spraying, both the CC and the GA coatings exhibited fewer low-temperature thermal events compared to the starting powders, as shown in Fig. 11. The thick and thin coatings of CC powder have a small amount of ω decomposition, which is not observed in the GA powder coatings. The onset of melting at approximately 900 °C is nearly constant for all the coatings, which indicates that the composition of the ψ phase is consistent from coating to coating. The behavior above the onset of melting is different for the CC and GA materials, showing that the proportion of the high-temperature phases—λ and β—is different, contrary to Fig. 8.

4. Discussion

The contrasting cooling rates experienced by the CC and GA powders produced significantly different solidification microstructures for the Al-Cu-Fe alloy studied. The degree of chemical segregation is the most visible difference, but this would be expected with the peritectic reactions that are characteristic of

Table 4 EDS data taken at the numbered spots shown in Fig. 9(c)

Spot number(a)	Al, at.%	Cu, at.%	Fe, at.%
1	73.9	7.0	19.2
2	62.9	23.4	13.7
3	72.7	8.1	19.2
4	75.1	6.7	18.3
5	68.4	20.4	11.2

(a) Spots 1, 3, and 4 closely correspond to the λ phase, whereas spots 1 and 2 correspond to the β phase.

the Al-Cu-Fe system. Apparently, even the rapid solidification history of the atomized powders was not able to bypass the peritectic reaction and its resulting segregation. The structures of the phases formed in the two powders are similar, although the slower cooling of the original ingot from which the CC powder was formed provided the opportunity to form the lower-melting-temperature θ phase. The macroinhomogeneities developed in the chill-cast ingot of the $Al_{63}Cu_{25}Fe_{12}$ composition are seen by comparing Fig. 1 and 5. Individual particles produced by crushing the cast ingot into a 5 to 45 μm particle size distribution can have completely different chemical compositions and crystalline structures. These inhomogeneities are clearly demonstrated in the SEM micrographs of Fig. 1 and the DTA traces of Fig. 10. The differences in chemical homogeneity between the CC and GA powders are retained in coatings formed from both types.

The DTA analyses are more indicative of the relative fractions of the various phases. Curve (b) in Fig. 10 shows a slight indication of reactions from the θ and ω phases for the GA powders, which confirms that the majority of the material comprises the ψ and β phases. The apparent significance of the prominent β peak in the XRD pattern shown in Fig. 5(b) is due to structure factor considerations. The β phase is body-centered cubic (bcc) and thus has only a few strong scattering planes. Conversely, the ψ and λ phases have numerous planes that have small scattering factors. Therefore, direct correlation of phase content based on peak areas or intensities can be misleading. Based on these observations, it appears that the GA powders have higher fractions of the ψ and β phases than the CC powders and coatings. However, these differences are not as pronounced in the plasma-sprayed coatings.

Comparison of the XRD traces obtained from sprayed coatings with TEM micrographs reveals an apparent anomaly. The XRD results in Fig. 8 indicate the presence of two phases: ψ and β. However, the bright-field TEM images in Fig. 9 show that the monoclinic λ phase is present in both the CC and GA powder coatings. It is quite possible that this result is due to chemical variations of the individual phases, particularly λ and β. The strongest reflections for the ψ, β, and λ structures are centered around a close range of 2θ values between 44 and 46°. Extensive substitutional solid solution could make resolution of individual planar reflections very difficult, depending on peak shifting. Evidence of variable phase compositions is also indicated by the data shown by curve (a) in Fig. 8. The peaks appear to have broadened in the CC powder coating. Typically, this effect would be due to small grain sizes (i.e., <1 μm). However, the ap-

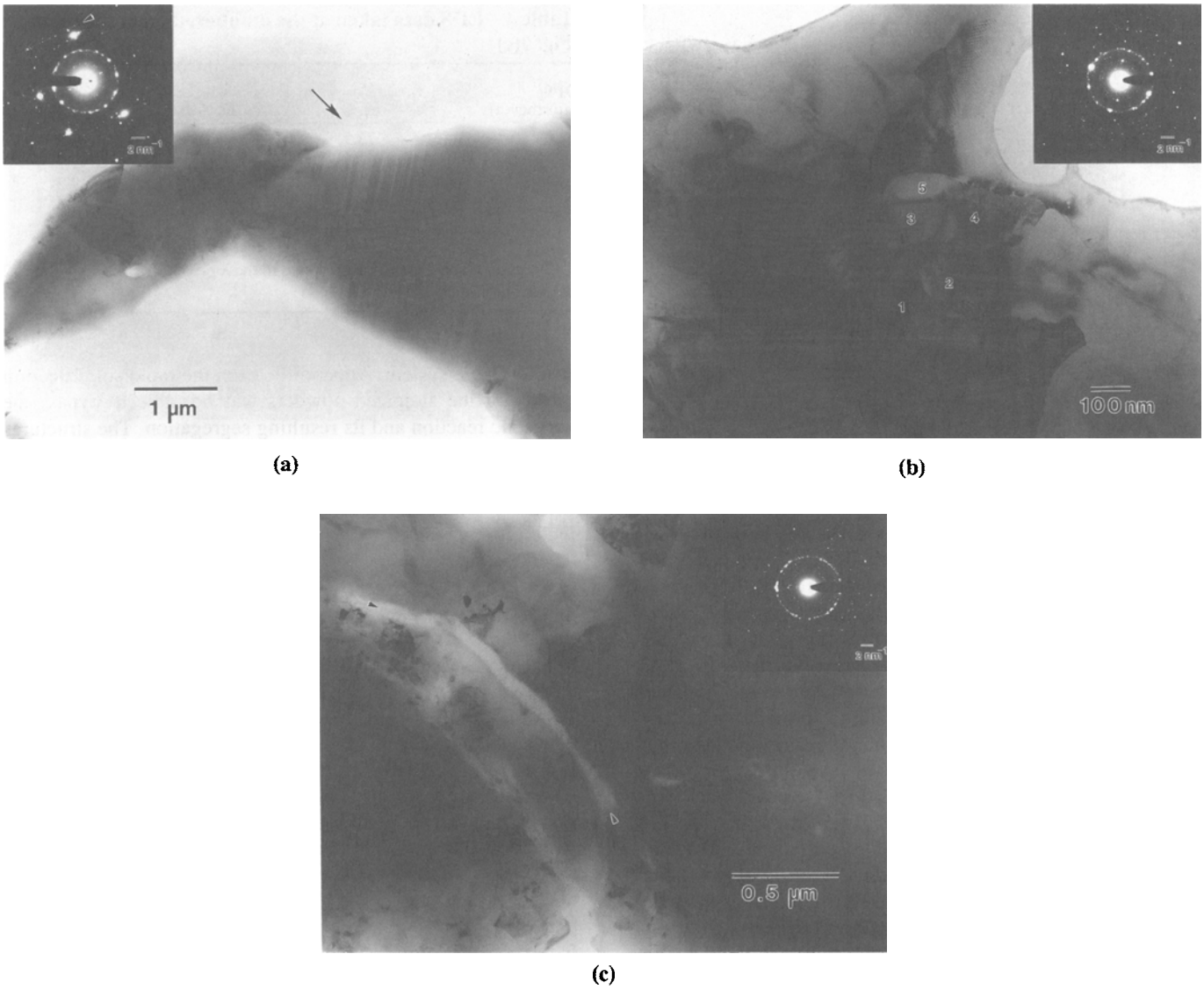

Fig. 9 Bright-field TEM micrographs of plasma-sprayed coatings. (a) Planar section of CC powder showing a large λ grain (arrow) and corresponding diffraction pattern (arrow on inset). (b) Planar section of GA powder showing a much finer grain-size distribution for the crystalline phases. The numbered grains correspond to EDS points displayed in Table 4. (c) Cross section of GA powder showing the amorphous aluminum-rich region (arrow) in between the fine polycrystalline regions. Inset is a SADP showing ψ, β, and λ phases

parent grain size, particularly in the crystalline phases, was too large to create this effect. Compositional variations could produce the integrated peak shifting seen in the XRD scan. This effect would make the resolution of ψ, β, and λ peaks even more difficult if the phases exhibiting substitutional solid solution were present in a range of stoichiometries. Subtle peak shifts from these deviations in phase chemistries could bring adjacent peaks even closer together.

Thus far, attention has been focused on the differences between the CC and GA powders and the coatings obtained from them. The GA powders are clearly more homogeneous than the CC powders; however, they still result in a multiphase coating. The individual splat shown in Fig. 6 helps to illustrate the barrier to directly forming a single-phase structure with the Al-Cu-Fe system. The very fine grain structure is a precursor for the larger grains that form during plasma spraying. The particular CC splat analyzed has a metastable structure. The cubic structure of the splat is similar to the β phase observed in the powders and coatings, but it appears to be highly disordered. It could not be indexed to a bcc lattice. Because the splat was formed from the CC powder, it is possible that the individual particle that formed the splat was rich in β phase. Nevertheless, the disordered structure still must evolve to the structure seen in the plasma-sprayed coatings. This evolution is likely a solid-state diffusion phenomenon. The heat provided by incoming molten particles together with the heat liberated during solidification provides the energy to activate the microstructural development. If the splat solidification process is indeed characteristic of the Al-Cu-Fe

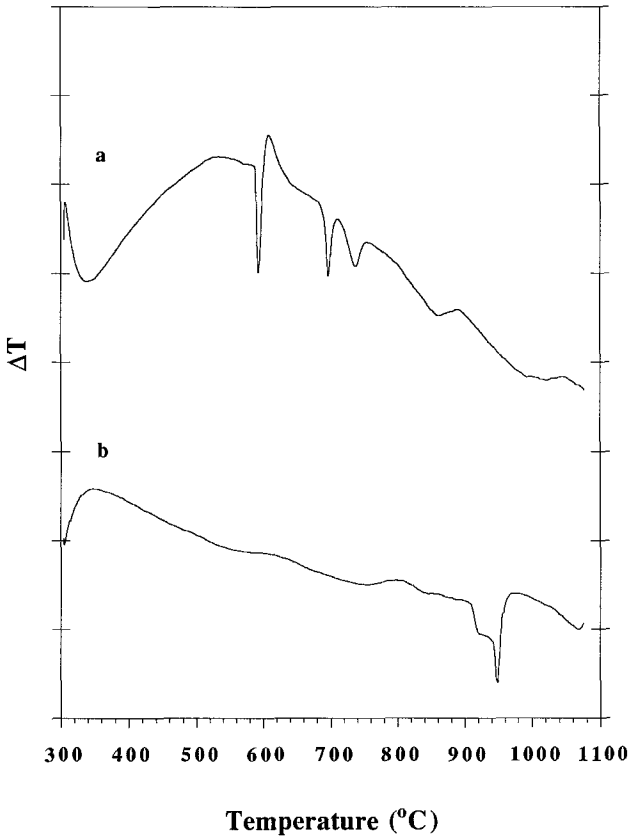

Fig. 10 DTA scans of CC powder (a) and GA powder (b). The exothermic reactions are discussed in the text

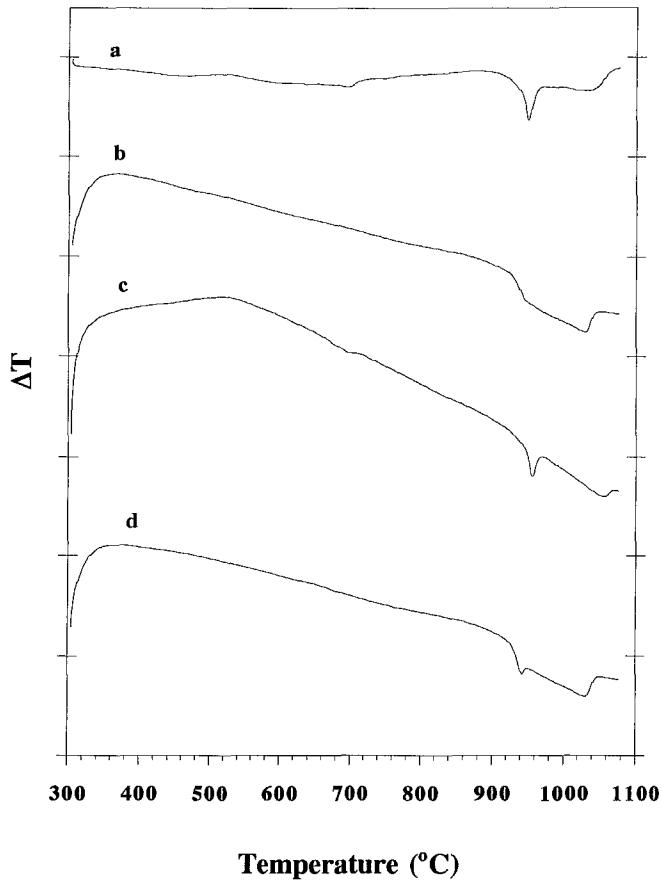

Fig. 11 DTA scans of a CC thin coating (a), a GA thin coating (b), a CC thick coatings (c), and a GA thick coating (d). All show the same melting temperature of the ψ phase, but different high-temperature behavior

system, which has a very complex solidification path, then it would be desirable to produce powder having an even finer degree of chemical homogeneity than that of the GA powders examined in this study.

5. Conclusions

The complex phase equilibrium relationships of the Al-Cu-Fe system make powder synthesis by solidification processes strongly dependent on cooling rates. Casting and crushing an $Al_{63}Cu_{25}Fe_{12}$ alloy ingot produced large-scale phase separation compared to rapid solidification. Solidification of the $Al_{63}Cu_{25}Fe_{12}$ composition yields a multiphase alloy that contains a quasi-crystalline phase very close to the starting composition and several ternary intermetallic phases. The powder solidification microstructure characteristics were clearly reflected in the final plasma-sprayed coating microstructures. Cast and crushed powder yielded chemically inhomogeneous coatings with large (>1 μm) grain sizes. On the other hand, rapidly solidified powder produced more chemically uniform coatings with much finer grain sizes.

Acknowledgments

The authors would like to thank L.P. Lincoln and M.F. Besser for their respective technical expertise in preparing the ingot castings and performing the plasma spraying. The efforts of I.E. Anderson and R. Terpstra in synthesizing the rapidly solidified powder also are acknowledged. This study was performed at the Ames Laboratory, Iowa State University, and was supported by the director of Energy Research, Office of Basic Sciences, United States Department of Energy, under Contract No. W-7405-ENG-82.

References

1. U. Köster, W. Liu, H. Leibertz, and M. Michel, Mechanical Properties of Quasicrystalline and Crystalline Phases in Al-Cu-Fe Alloys, *J. Non-Cryst. Solids,* Vol 153/154, 1993, p 446-452
2. J.M. Dubois, S.S. Kang, and J. Von Stebut, Quasicrystalline Low-Friction Coatings, *J. Mater. Sci.,* Vol 10, 1991, p 537-541
3. S.S. Kang, J.M Dubois, and J. Von Stebut, Tribological Properties of Quasicrystalline Coatings, *J. Mater. Res.,* Vol 8 (No. 10), 1993, p 2471-2481
4. E. Kubel, Jr., Powders Dictate Thermal Spray Coating Properties, *Adv. Mater. Process.,* Vol 138, 1990, p 24-26
5. D.L. Houck, Techniques for the Production of Flame and Plasma Spray Powders, *Mod. Devel. Powder Metall.,* Vol 12-14, 1980, p 485-504
6. D. Chauxian, R.A. Zatorksi, H. Herman, and D. Oh, Oxide Powders for Plasma Spraying—The Relationship between Powder Characteristics and Coatings Properties, *Thin Solid Films,* Vol 118, 1984, p 467-475

7. E. Lugscheider and I. Rass, Underwater Plasma Spraying of Stabilized Zirconia for Thermal Barrier Coatings, *J. Therm. Spray Technol.*, Vol 1 (No. 1), 1992, p 49-56
8. M. Yasuda, F. Weinberg, and D. Tromans, Pitting Corrosion of Al and Al-Cu Single Crystals, *J. Electrochem. Soc.*, Vol 137, 1990, p 3708-3715
9 F.W. Gayle, A.J Shapiro, F.S. Biancaniello, and W.J. Boettinger, The Al-Cu-Fe Phase Diagram: 0 to 25 At. Pct Fe and 50 to 75 At. Pct Al—Equilibria Involving the Icosahedral Phase, *Metall. Trans. A*, Vol 23A, 1992, p 2409-2417
10. D. Gratias, Y. Calvayrac, J. Devaud-Rzepski, F. Faudot, M. Harmelin, A. Quivy, and P.A. Bancel, The Phase Diagram and Structures of the Ternary Al-Cu-Fe System in the Vicinity of the Icosahedral Region, *J. Non-Cryst. Solids*, Vol 153/154, 1993, p 482-488
11. J. Shield, University of Utah, private communication